Grading the amount of electrochemcial active sites along the main flow direction of an SOFC

Andersson, Martin; Yuan, Jinliang; Sundén, Bengt

Published in:
Journal of the Electrochemical Society

DOI:
10.1149/2.026301jes

2013

GRADING THE AMOUNT OF ELECTROCHEMICAL ACTIVE SITES ALONG THE MAIN FLOW DIRECTION OF AN SOFC

Martin Andersson*, Jinliang Yuan and Bengt Sundén
Department of Energy Sciences, Faculty of Engineering,
Lund University, Box 118, 221 00 Lund, Sweden

* Corresponding author:
Martin.Andersson@energy.lth.se
+46 46 222 4908

ABSTRACT

A fully coupled computational fluid dynamics (CFD) approach based on the finite element method, in two-dimensions, is developed to describe a solid oxide fuel cell (SOFC). Both hydrogen and carbon monoxide are considered as electrochemical reactants within the anode. The dimensionless number of electrochemical active sites (EAS), the pore radius (indirectly proportional to the particle radius) and the active area-to-volume ratio available for methane reforming are graded, along the main flow direction, to equalize the current density distribution. Previous studies available in the open literature only considered grading in the direction normal to the main flow direction, in terms of porosity and tortuosity. It is found that grading the active area-to-volume ratio available for methane reforming increases the OCV along the main flow direction. It is concluded that an optimized graded EAS reduces the need of air flow rate with 21 %, with the same outlet temperatures as for the ungraded case.

Keywords: *SOFC, Modeling, Cell scale, 2D, Grading, Dimensionless number of electrochemical active sites, Pore radius.*

INTRODUCTION AND PROBLEM STATEMENT

Fuel cells (FCs) are promising candidates for providing electrical power for future energy systems due to the high efficiency values and low emissions of NO_x compared to conventional power generation systems [1-2]. The solid oxide fuel cell (SOFC) is a high temperature fuel cell which operates at temperatures between 600-1000°C [3]. The ability of working at these high temperatures allows SOFCs to operate with different types of fuels no matter they come from a fossil or a renewable source. Moreover, SOFCs are more tolerant to contaminants than other FCs and they are capable of reforming the fuel internally or externally making them interesting candidates for power generation. In fact, the capability of reforming hydrocarbon fuels promotes SOFCs as prime candidates for leading the transition from conventional power generation with hydrocarbon based fuels to fuel cells which can operate under a wide range of fuels, especially those coming from renewable resources [1].

If hydrogen and/or carbon monoxide are supplied as fuel, no reforming process is required as they can be directly used as reactants. Thus, considering hydrogen and carbon monoxide as fuel, the reactions that take place within SOFCs can be globally described as follows: Oxygen is reduced at the cathodic three-phase boundary (TPB), as in eqn (1). The oxygen ions are transported through the electrolyte, but the electrons are prevented to pass through it. The electrochemical reactions between hydrogen and oxygen ions, eqn (2) as well as between carbon monoxide and oxygen ions, eqn (3), take place in the anodic TPB [4-5].

$$\frac{1}{2}O_2 + 2e^- \rightarrow O^{2-} \tag{1}$$

$$H_2 + O^{2-} \rightarrow H_2O + 2e^- \tag{2}$$

$$CO + O^{2-} \rightarrow CO_2 + 2e^- \tag{3}$$

When a fuel containing methane or carbon monoxide, i.e., the main components of natural gas is supplied, the reforming takes place within the anode. Methane is reformed with steam (eqn (4)), the so-called methane steam reforming reaction (MSR). Carbon monoxide can be oxidized in the electrochemical reaction (eqn (3)) and also reacts with water (eqn (5)), the so-called water-gas shift reaction (WGSR) [4]. The reactions described here are the overall ones, more detailed reaction mechanisms can be found in [5].

$$CH_4 + H_2O \Leftrightarrow 3H_2 + CO \qquad \text{(MSR, 4)}$$

$$CO + H_2O \Leftrightarrow H_2 + CO_2 \qquad \text{(WGSR, 5)}$$

The electrochemical reactions in SOFC composite electrodes take place in the TPB region, where the ion conducting particles meet with electron conducting particles and also the pores containing gas-phase species. To

enable electrochemical reactions the ion and electron conductors must also be in contact with their corresponding base, i.e., the current collector in case of electron conducting materials and electrolyte in case of ion conducting materials, through other particles of the same type [6]. SOFC electrochemical behavior is mainly determined by the reaction activation-, ohmic- and concentration polarizations. The respective polarizations are strongly influenced by the microstructure of the electrodes and depend on the quantity and location of the TPBs, i.e., the SOFC performance can be improved by modifying the electrode microstructures [7]. Grading the porous microstructure can be applied to improve the electrochemical characteristics of the cell.

Greene *et al.* [8] grades the porosity-tortuosity ratio through the electrodes, in the direction normal to the main flow direction, and concludes that the performance benefits take place when the electrodes have a higher porosity near the electrolyte interface. It is also shown that the methane reforming reaction is enhanced by high tortuosity structures due to the increased residence time for the gas molecules within the electrodes. Ni *et al.* [4,9] found that the micro-structural grading (in the direction normal to the main flow direction) could significantly enhance the gas transport. However, the effects on activation and ohmic polarizations were found to be small for thick electrodes. It was found that particle size grading is typically more effective than porosity grading to increase the power density. Deseure *et al.* [10] grades the cathode composition (in the direction normal to the main flow direction) to decrease the ion transport resistance. Schneider *et al.* [11] grades the ion conducting volume fraction through the electrodes, in the direction normal to the main flow direction, to reduce the thermal mismatch stresses between the fuel cell components and also to optimize the electronically and ionically conductive networks. The conductive network can be optimized due to the fact that electron and ion currents flow at the opposite ends of the electrodes. Shi and Xue [12] developed a computational fluid dynamics (CFD) model for a bi-layered electrode supported cell with a porosity grading through the electrodes in the direction normal to the main flow direction. Linear as well as non-linear distributions of the electrode porosity are compared and it is concluded that the inverse parabolic porosity shows the most promising effect on cell performance. Liu *et al.* [7] grades the porosity as well as the particle size, in the direction normal to the main flow direction, in order to enhance the cell performance. Overall, the particle size grading was found to be more effective to decrease the polarizations in an SOFC anode, compared to porosity grading. In practice, the porosity- or pore radius (in the direction normal to the main flow direction) graded electrodes can be manufactured by advanced ceramic techniques or by electrophoretic co-deposition [9,13]. “A manufacturing technique for the electrodes, which are graded along the main flow direction, is the computer aided fabrication technique called n-Scrypt. However, this is outside the scope of this article”.

This study aims to investigate the impact from a graded dimensionless number of electrochemical active sites (EAS) structure and pore radius along the main flow direction (i.e., x-direction for the model used in this work, as shown in Fig. 1). The EAS are defined as a correction factor to the active surface area-to-volume ratio in the source terms in the governing equations for ion and electron transport, i.e., also directly proportional to the electrochemical reaction rate. Previous studies available in the open literature investigated graded structures through the electrodes in the direction normal to the main flow direction only (i.e., y-direction as in this work). However, it is expected that grading along the main flow direction is also an important step to increase the electrochemical efficiency as well as to enhance the scientific understanding concerning the different polarizations and their influences on the SOFC performance. To the authors' knowledge, grading of the EAS and the pore radius along the main flow direction (x-direction), as employed in this study, is unique. Porosity and/or particle radius (indirectly proportional to the pore radius) grading through the electrodes in the direction normal to the main flow direction (y-direction) is commonly applied within various studies in the open literature.

MATHEMATICAL MODEL

A two-dimensional (2D) model for an anode-supported SOFC is developed and implemented in the commercial software COMSOL Multiphysics (version 4.2a), based on FEM (finite element method). Equations for momentum, gas-phase species, ion, electron and heat transport are solved simultaneously. As our model is defined in 2D only, i.e., the calculation is for a domain at the mid-plane of a unit cell. In reality, the current density will be higher in the middle of the electrodes. The geometry, based on a standard cell at the Ningbo Institute of Material Technology and Engineering (NIMTE) in China, is defined in Table 1, and a sketch of the investigated cell can be seen in Fig. 1. Note that Fig. 1 is not to scale.

Table 1: Cell geometry

Figure 1: Sketch of an anode-supported SOFC, not to scale.

Grading of the EAS

In this work the EAS, within the electrodes, are graded along the main flow direction (i.e., the x-direction in the model developed in this study), as presented in Fig. 2. The EAS is implemented in the model as a correction factor to the active surface area-to-volume ratio in the source terms in the governing equations for ion and electron transport, to cover the electrochemical reactions. The physical meaning of grading is to vary the pore and particle size in the direction along the main flow direction, i.e., the surface area available for the electrochemical reactions differs along

the main flow direction. Note also that the source terms due to electrochemical reaction for gas-phase species, momentum and heat transport equations are affected by the EAS grading. The grading is aimed to equalize the current density distribution along the main flow direction. An equalized current density is expected to decrease the heat generation due to ohmic polarization, because of the direct square proportionality to current density. Note that the same grading is applied within the anode and the cathode. It should be noted that grading can be applied for the porosity, keeping the (average) pore radius constant, but also for the (average) pore radius, keeping the porosity constant. Both the porosity and the pore size can be graded simultaneously for extended structure optimization [4]. However, it is in this study assumed that the porosity as well as tortuosity are kept constant. Grading the electrode porosity and tortuosity would affect the governing equations describing ion, electron, momentum, gas-phase species and heat transport.

The different cases in Fig. 2 are: **A** is for the ungraded case, **B** for the EAS being inversely proportional to the position along the main flow direction and **C** for the EAS being optimized along the main flow direction to minimize the change in current density along the main flow direction. The EAS on the y-axis is dimensionless and "1" corresponds to the number of electrochemical active sites before the grading approach is implemented. Note that the mean value of the EAS equals unity for all cases studied. Obviously a higher mean value of EAS would increase the cell performance even further.

The pore- and particle radius are related to each other by eqn (6) [12], when assuming a uniform pore- and particle size distribution in the direction normal to the main flow direction in this study. An expected advantage with EAS grading, i.e., increasing the pore radius, along the main flow direction is that the anode concentration polarization reduces, because the mass transport resistance decreases as the pore size increases along the main flow direction. The effect of pore and particle size on the electrochemical reactions at TPB is outlined in the open literature [4,6,12] as presented in eqns (6-8) and in Fig 3 (relating to case **C** in Fig. 2). The EAS is defined to be directly proportional to the electrochemical reaction rate (eqn (7)) and assumed to be directly proportional to the active area-to-volume ratio covering the TPB region. The pore radius is inversely proportional to the EAS, based on that the electrochemical reaction rate is directly proportional to the active surface area available for the electrochemical reactions [4,6,12] (see eqn (8)). Note that the number of pores and particles increases as the radius decreases. An alternative approach to define the relationship between the electrochemical reaction rates and the structure includes the TPB length (instead of TPB area as employed within this study). However, the electrochemical reaction rates are still assumed to be inversely proportional to the pore radius [9], i.e., the relationship between the electrochemical

reaction rate and pore radius employed in this study is still valid. As the active area-to-volume ratio in the anode for the MSR is graded it is assumed that it is direct proportional to the MSR, i.e., implemented as for the EAS.

$$r_{pore} = \frac{2}{3} \cdot r_{particle} \cdot \varepsilon \cdot (1-\varepsilon)^{-1} \tag{6}$$

$$r_e \propto EAS \propto AV_e \tag{7}$$

$$AV_e \propto \frac{1}{r_{particle}} \propto \frac{1}{r_{pore}} \tag{8}$$

where ε is the porosity, r_{pore} the average pore radius, $r_{particle}$ the average particle radius, AV_e the active area-to-volume ratio available for electrochemical reactions and r_e the electrochemical reaction rate. Notice, the AV_e is lower than the total surface area of the sintered solid materials, because only a fraction of the total area is considered to be active, and also that it differs from the active area available for the methane steam reforming reaction within the anode.

Figure 2: Grading the EAS along the main flow direction

Figure 3: Distribution of the dimensionless pore radius along the main flow direction, assuming that the pore radius is directly proportional to the active surface area, compared to the ungraded case.

Ion and electron transport

The potential difference between the anode and the cathode current collectors corresponds to the total cell voltage (V_{cell}). The governing equations for the ion and electron transport are implemented as:

$$i_{el} = \nabla \bullet \left(-\sigma_{el,YSZ} \nabla \phi_{el} \right) \tag{9}$$

$$i_{io} = \nabla \bullet \left(-\sigma_{io,Ni/\mathrm{LSM}} \nabla \phi_{io} \right) \tag{10}$$

where ϕ is the potential, σ the ionic/electronic conductivity, i the ion/electron current density, *el* is the index for the electrolyte material (YSZ) and *io* for the electron conducting materials (Ni or LSM). The potential at the anode current collector is set to zero and the potential at the cathode current collector is set as the cell operating voltage (V_{cell}

=0.7 V in this study). All other boundaries and interfaces are electrically insulated. The electronic conductivities in the anode and the cathode as well as the ionic conductivity in the electrolyte material are calculated as [14-15]:

$$\sigma_{io,LSM} = 4.2 \cdot 10^{7} \cdot T^{-1} \cdot \exp\left(-1200 \cdot T^{-1}\right) \tag{11}$$

$$\sigma_{el,YSZ} = 33.4 \cdot 10^{3} \cdot \exp\left(-10300 \cdot T^{-1}\right) \tag{12}$$

$$\sigma_{io,Ni} = 9.5 \cdot 10^{7} \cdot T^{-1} \cdot \exp\left(-1150 \cdot T^{-1}\right) \tag{13}$$

where T is the temperature. The ions and electrons can not be transported in straight paths in the electrodes, because the transport distances increase due to the real/functional material compositions and their micro structures. This is accounted for by using the structure dependent tortuosity factors and volume fractions, as presented in [27]. Note that the tortuosity for ion and electron transport differs from the tortuosity for gas-phase transport.

The Nernst potential or the electromotive force (reversible open-circuit voltage, E^{OCV}) is determined by the difference in thermodynamic potentials of the electrode reactions. When a hydrogen-steam mixture is used as fuel, it can be calculated by the Nernst equation (eqn (14)) [16-17]. The electromotive force for carbon monoxide as fuel is presented in eqn (16) [18]. It should be noted that it is assumed that the OCV equals the theoretical voltage.

$$E_{H_2/O_2}^{OCV} = E_{H_2/O_2}^{0} - \frac{1}{2} \cdot \mathrm{R} \cdot T \cdot F^{-1} \cdot \ln\left(p_{H_2O} \cdot {p_{H_2}}^{-1} \cdot {p_{O_2}}^{-1/2}\right) \tag{14}$$

$$E_{H_2/O_2}^{0} = 1.253 - 2.4516 \cdot 10^{-4} \cdot T \tag{15}$$

$$E_{CO/O_2}^{OCV} = E_{CO/O_2}^{0} - \frac{1}{2} \cdot \mathrm{R} \cdot T \cdot F^{-1} \cdot \ln\left(p_{CO_2} \cdot {p_{CO}}^{-1} \cdot {p_{O_2}}^{-1/2}\right) \tag{16}$$

$$E_{CO/O_2}^{0} = 1.46713 - 4.527 \cdot 10^{-4} \cdot T \tag{17}$$

where E^0 is the temperature dependent OCV at standard pressure and p_i the partial pressure, at the TPB, in atm. Even with several reactions, only one OCV can occur simultaneously, i.e., an averaged value is estimated to represent the one achieved at $H_2/CO/CO_2/H_2O$ environment, such as the case in this study, according to:

$$E_{avg}^{OCV} = E_{H_2/O_2}^{OCV} \cdot x_{H_2} \cdot \left(x_{H_2} + x_{CO}\right)^{-1} + E_{CO/O_2}^{OCV} \cdot x_{CO} \cdot \left(x_{H_2} + x_{CO}\right)^{-1} \tag{18}$$

where x is the mole fraction of the respective species.

It should be mentioned that the expressions for the OCV for hydrogen and for carbon monoxide are developed for simplified pure mixtures. Suitable OCV expressions specific for more complex fuel mixtures are interesting to develop further in future models. Notice, for this study (with 30 %- pre reformed natural gas as fuel) the OCV for

hydrogen and for carbon monoxide does not differ more than 0.01 V at any position. However, for other fuel compositions the difference can be much bigger.

Due to internal resistance and polarizations the actual voltage (E) becomes less than the OCV. E can be expressed as [19]:

$$E = E_{avg}^{OCV} - \eta_{act} - \eta_{ohm} - \eta_{conc} \tag{19}$$

where η is the respective polarization. The activation polarizations are defined as [20-22]:

$$\eta_{act,a} = \phi_{io} - \phi_{el} \tag{20}$$

$$\eta_{act,c} = \phi_{io} - \phi_{el} - E_{avg}^{OCV} \tag{21}$$

where the index a stands for the anode and c for the cathode. Note that the activation polarizations in eqns (20)-(21) are connected to the validated expressions describing the local current density in eqns (30)-(32), including, e.g., the local temperature and concentrations. The concentration polarizations are specified as [23]:

$$\eta_{conc,a,H_2} = \mathrm{R} \cdot T \cdot n_{e,a}^{-1} \cdot \mathrm{F}^{-1} \cdot \ln\left(p_{H_2O,TPB} \cdot p_{H_2,b} \cdot p_{H_2,TPB}^{-1} \cdot p_{H_2O,b}^{-1}\right) \tag{22}$$

$$\eta_{conc,a,CO} = \mathrm{R} \cdot T \cdot n_{e,a}^{-1} \cdot \mathrm{F}^{-1} \cdot \ln\left(p_{CO_2,TPB} \cdot p_{CO,b} \cdot p_{CO,TPB}^{-1} \cdot p_{CO_2,b}^{-1}\right) \tag{23}$$

$$\eta_{conc,c} = \mathrm{R} \cdot T \cdot n_{e,a}^{-1} \cdot \mathrm{F}^{-1} \cdot \ln\left(p_{O_2,b} \cdot p_{O_2,TPB}^{-1}\right) \tag{24}$$

where $p_{i,TPB}$ stands for the partial pressure at TPB, $p_{i,b}$ the partial pressure at the interface between the gas channel and the electrode, R is the gas constant and F is the Faraday constant. Note that the expressions for concentration polarizations within the anode do not include methane, neither the influence from carbon monoxide and carbon dioxide in the hydrogen concentration polarization (eqn (22)), nor the influence from hydrogen and water in the carbon monoxide concentration polarization (eqn (23)).

Momentum transport

The gases flow inside the fuel cell components, such as in the air and fuel channels, and in the porous electrodes. Equation (25) is introduced and solved for the gas flow in the fuel and air channels and in the porous materials simultaneously [24-25], i.e., the interface conditions between the gas channels and the porous electrodes do not need to be defined, according to the so-called Darcy-Brinkman equation. It should be noted that Liu *et al.* [26] used

COMSOL Multiphysics and eqn (25) (as employed in this work) to confirm similar result achieved by the commercial software Fluent applying the FVM (finite volume method).

$$\rho_g \cdot \varepsilon^{-1} \cdot (\nabla \bullet \vec{u}) \cdot \vec{u} \cdot \varepsilon^{-1} - \nabla \left[-p + \mu_g \cdot \varepsilon^{-1} \left\{ \Psi - \frac{2}{3} (\nabla \bullet \vec{u}) \right\} \right] + \left(\mu_g . \kappa^{-1} + \beta_F |\vec{u}| + \nabla (\rho_g \cdot \vec{u}) \cdot \vec{u} \right) = \mathbf{F} \tag{25}$$

In eqn (25) **F** is the volume force vector, κ the permeability of the porous medium ($1.76 \cdot 10^{-11}$ m^2), $\vec{u}$ the velocity vector, Ψ the viscous stress tensor and β_F the Forchheimer coefficient (includes the microscopic inertial effects)**.** The density (ρ_g) and viscosity (μ_g) for the participating gas mixtures are dependent on local mole fractions and temperature, as described in [27]. The momentum equation in the air and fuel channels reduces to eqn (26) [25]:

$$\rho_g \cdot (\nabla \bullet \vec{u}) \cdot \vec{u} - \nabla \left[-p + \mu_g \cdot \left\{ \Psi - \frac{2}{3} \cdot (\nabla \bullet \vec{u}) \right\} \right] = \mathbf{F} \tag{26}$$

The gas inlet velocities are defined as developed laminar flow profiles, and the average values are based on the fuel and oxygen utilization, i.e., 71 % and 13 %, respectively, for the case with no grading. As a graded structure is implemented the flow rates are kept constant, i.e., the fuel and oxygen utilizations are not specified directly for these cases. At the outlets, the pressure (1 atm) is fixed.

Gas-phase species transport

In the porous material, there are two kinds of gas-phase species diffusion mechanisms; molecular (collisions between two different gas molecules) and Knudsen (collisions between the gas molecules and the pore walls) diffusions. The Knudsen diffusion coefficients ($D_{k,ij}$) are calculated based on the free molecule flow theory, as described in [28]. Notice, the pore radius is graded along the main flow direction as a function of the EAS, as described in eqns (6)-(8), and implemented in the model as a correction factor multiplied with the original pore radius for one case in the parameter study. For a multi-component gas mixture system, the temperature dependent binary diffusion coefficients (D_{ij}) are calculated by the expressions in [29], based on binary-component coefficients of the gases. In the porous media, there is an increased diffusion length due to the tortuous paths of local connected pores and the coefficients are usually corrected by porosity and tortuosity (τ) [28,30]:

$$D_{eff,ij} = \varepsilon \cdot \tau^{-1} \left(D_{ij} \cdot D_{k,ij} \cdot \left(D_{ij} + D_{k,ij} \right)^{-1} \right) \tag{27}$$

Equation (27) is used to describe the gas-phase species transport phenomena for each component inside the cell [25] and solved for the fuel and air channels and for the electrodes.

$$\nabla\left(-\rho\cdot w_i\sum_{j\neq i}^{n}D_{eff,ij}\cdot\nabla x_j+\left(x_j-w_j\right)\cdot\nabla p\cdot p^{-1}\bullet\vec{\mathrm{u}}-D_i^T\cdot\nabla T\cdot T^{-1}\right)+\rho\cdot\vec{\mathrm{u}}\cdot\nabla w_j=S_i \tag{28}$$

Here w is the mass fraction, n the number of species and D_i^T the thermal diffusion coefficient. S_i, the mass source term due to chemical reactions, is defined for the internal reforming and the electrochemical reactions. The eqn (28) is solved for O_2 and N_2 on the cathode side as well as for ten different pairs of H_2, CO, CO_2, H_2O and CH_4 on the anode side.

The anode inlet conditions are defined as 30 % pre-reformed natural gas, as specified by International Energy Agency (IEA) and frequently found in the open literature, i.e., $x_{H2} : x_{CH4} : x_{CO} : x_{H2O} : x_{CO2} = 0.2626 : 0.171 : 0.0294 : 0.4934 : 0.0436$ [3]. The cathode inlet is defined as air, including oxygen and nitrogen. The boundary conditions for the outlets are defined as convective flux.

Heat transport

A local temperature equilibrium (LTE) approach is applied, i.e., the temperature is assumed to be locally the same for the gas and solid-phases (within the electrodes). Previously a local temperature non-equilibrium (LTNE) approach has been applied [3]. However, the temperature difference between the solid and gas-phases within the electrodes is found to be neglible for the investigated cases. The governing equation for the temperature distribution in this work is defined as:

$$\rho_g\cdot c_{p,g}\cdot\vec{\mathrm{u}}\cdot\nabla T=\nabla\bullet\left(k_{eff}\nabla T\right)+Q_h \tag{29}$$

where Q_h is the heat generation/consumption, k_{eff} the effective thermal conductivity and $c_{p,g}$ the gas-phase specific heat. The overall governing equation for the heat transport reduces to pure heat conduction in the electrolyte and in the interconnector. The respective source terms due to the internal reforming reactions, ohmic-, activation- and concentration polarizations as well as the change of entropy due to the electrochemical reactions are presented in [27]. Note that eqn (29) is continuous over the gas channel/interconnect interfaces due to the LTE approach, as applied in this work, i.e., no heat supplies or heat sinks need to be defined at these interfaces.

The inlet gas temperature is defined by the operating temperature (1000 K) and the outlet is defined as convective flux. The boundaries at the top and the bottom of the cell are defined as symmetry conditions, because it is assumed that the cell is surrounded by other ones with identical temperature distribution.

Electrochemical reactions

The current density is calculated separately at the anodic side for hydrogen and carbon monoxide according to the approach developed by Suwanwarangkul *et al.* [22], as presented in eqns (30)-(32). The rate of oxygen reduction at the cathode is determined by the rate of oxygen adsorption as the rate-determining step. Independent on the number of electrochemical reactions, only one OCV can exist, as discussed above. Note that this electrochemical approach also includes the gas-phase partial pressures, which are frequently neglected within the open literature and also in our previous models [3,27,31]. The current approach assumes that the pre-exponential factor of the CO oxidation reaction is 2.5 times lower than that of the H_2 oxidation reaction, because the CO oxidation presents a much higher activation polarization than for the H_2 oxidation reaction at the same current density. This assumption can be compared to the result from Matsuzaki and Yasuda [32], where it was concluded that the electrochemical oxidation rate of H_2 at the interface in a porous Ni-YSZ cermet electrode and YSZ electrolyte is 1.9-2.3 times higher than that of CO at 1023 K and 2.3-3.1 times higher at 1273 K.

$$i_c = EAS \cdot AV_{e,c} \cdot 0.25 \cdot 10^{10} \cdot \exp\left(-130000 \cdot \mathrm{R}^{-1} \cdot \mathrm{R}^{-1} \cdot T^{-1}\right) \cdot \mathrm{R} \cdot T\sqrt{p_{O_2}} \cdot \mathrm{F}^{-1} \cdot \left[\exp\left(-2 \cdot \mathrm{F} \cdot \eta_{act,c} \cdot \mathrm{R}^{-1} \cdot T^{-1}\right) - \exp\left(2 \cdot \mathrm{F} \cdot \eta_{act,c} \cdot \mathrm{R}^{-1} \cdot T^{-1}\right)\right] \quad (30)$$

$$i_{a,H_2} = EAS \cdot AV_{e,a} \cdot 2.1 \cdot 10^{11} \cdot \exp\left(-120000 \cdot \mathrm{R}^{-1} \cdot T^{-1}\right) \cdot \mathrm{R} \cdot T \cdot p_{H_2O}^{0.266} \cdot \left(\mathrm{F} \cdot \left(K_{eq,H_2} \cdot p_{H_2}\right)^{0.266}\right)^{-1} \cdot \left[\exp\left(2 \cdot \mathrm{F} \cdot \eta_{act,a,H_2} \cdot \mathrm{R}^{-1} \cdot T^{-1}\right) - \exp\left(-\mathrm{F} \cdot \eta_{act,a,H_2} \cdot \mathrm{R}^{-1} \cdot T^{-1}\right)\right] \quad (31)$$

$$i_{a,CO} = EAS \cdot AV_{e,a} \cdot 0.84 \cdot 10^{11} \cdot \exp\left(-120000 \cdot \mathrm{R}^{-1} \cdot T^{-1}\right) \cdot \mathrm{R} \cdot T \cdot p_{CO_2}^{0.266} \cdot \left(\mathrm{F} \cdot \left(K_{eq,CO} \cdot p_{CO}\right)^{0.266}\right)^{-1} \cdot \left[\exp\left(2 \cdot \mathrm{F} \cdot \eta_{act,a,CO} \cdot \mathrm{R}^{-1} \cdot T^{-1}\right) - \exp\left(-\mathrm{F} \cdot \eta_{act,a,CO} \cdot \mathrm{R}^{-1} \cdot T^{-1}\right)\right] \quad (32)$$

In eqns (30)-(32) AV_e is the electrochemically active surface area-to-volume ratio and K_{eq} the temperature dependent equilibrium constant for eqns (2) and (3), respectively. The different K_{eq} are presented in [22] for 800 and 900 °C and it is assumed that the temperature dependence is linearly for the temperature range considered in this study. The implementation of eqns (30)-(32) includes fitting of the model (e.g., the values for AV_e) to experimental data performed at NIMTE (Ningbo Institute of Material Technology & Engineering) in China, as further described in [3,33].

The two electrochemical reactions (for H_2 and CO) are treated as two resistances in parallel [22,34]. Thus, the total local current density for the anode is calculated as the sum of the contributions of hydrogen and carbon monoxide anodic current densities, i.e.,

$$i_a = i_{a,CO} + i_{a,H_2} \tag{33}$$

The validity of equation (33) can be questioned since the intrinsic current, for example in [32], is not linear, indicates that hydrogen selectively adsorbs onto the nickel surface, and thus influences the adsorption of carbon monoxide. However, to the authors' knowledge, there is no any better (or complete) approach available in the open literature yet. The consideration of the influence of hydrogen and carbon monoxide on the current density contribution is interesting for future studies. Also the Butler-Volmer equations for SOFCs have been questioned recently [35-36]. The Butler-Volmer equations assume that the local field gradients are strong enough to perturb the energies of species along the reaction coordinate.

Internal reforming reactions

When a fuel containing methane and carbon monoxide is supplied, the reforming reactions take place within the anode. Methane reacts with steam in the MSR. Carbon monoxide can be oxidized in the electrochemical reaction, but also reacts with water in the WGSR [37]. The heat, which is generated within the cell (mainly from the electrochemical reactions), can be used for the internal steam reforming reaction within the anode and/or outside the cell for external reforming and pre-heating of the fuel and air. The reaction kinetics from Klein *et al.* [38] for the MSR (an Arrhenius form expression dependent on the active area-to-volume ratio) and from Haberman and Young [39] for the WGSR are used to calculate the reaction rates in this work, according to eqns (34)-(35). Note that the active area available for MSR is graded for the case in the parameter study. Other global kinetic models can be found in [40-41]. The catalytic methane steam reforming reaction occurs at the surfaces of the nickel catalysts, as specified [38]:

$$r_{MSR} = AV_{MSR} \cdot \left(943 \cdot \exp\left(-225 \cdot 10^3 \cdot R^{-1} \cdot T^{-1}\right) \cdot p_{CH_4} \cdot p_{H_2O} - 7.74 \cdot 10^{-9} \cdot \exp\left(-1937 \cdot R^{-1} \cdot T^{-1}\right) \cdot p_{CO} \cdot p_{H_2}^3\right) \tag{34}$$

where p_i is the partial pressure of gas species i. Equation (34) origins from the experiments performed at Research Centre Jülish, and the anode material consists of Ni−8YSZ substrate [42]. The range for the AV (for catalytic kinetic reactions) varies in the literature between $1 \cdot 10^5$ m^2/m^3 [43] and $2.2 \cdot 10^6$ m^2/m^3 [38] for SOFC anodes. The measured specific surface area for Ni/YSZ material developed for SOFC anodes is $70 \cdot 10^6$ m^2/m^3 in [44]. Note that not all the surfaces are available for the catalytic reactions, due to the distribution of catalyst, unavailable pores and mass transfer limitations among others. An AV of $10 \cdot 10^6$ m^2/m^3, corresponding to 14 percent of the total Ni/YSZ specific area to volume ratio, is used in this work. The trend for the FC development in recent years has been in the direction of employing smaller pores to get a larger AV.

Based on the global scheme for the anode, the expression for the catalyzed water-gas shift reforming reaction (WGSR, eqn (4)) in [39] has been selected in this study:

$$r_{WGSR} = k_{WGSR} \cdot \left(p_{H_2O} \cdot p_{CO} - p_{H_2} \cdot p_{CO_2} \cdot K_{WGSR}^{-1} \right) \tag{35}$$

The rate constant (k_{WGSR}) and the equilibrium constant (K_{WGSR}) are temperature dependent expressions calculated from the experimental data, as described in [39].

SOLUTION METHODS AND PARAMETERS APPLIED

All the equations, defined above, are numerically solved in COMSOL Multiphysics (version 4.2:1.166) using a stationary segregated solver with a direct (MUMPS) linear solver system. The governing equations are segregated in 5 different groups: **1.** velocity field, pressure distribution and pressure corrections, **2.** temperature distribution, **3.** ion and electron distribution, **4.** mass fraction distribution on the air side (O_2/N_2) and **5.** mass fraction distribution on the fuel side ($H_2/H_2O/CH_4/CO/CO_2$). The segregated solver solves for 2 390 000 degrees of freedom and the tolerance is defined to 0.0003 for each segregated group. Grid independence was achieved at 704 000 elements, after which the change in the maximum temperature is less than 0.01 %, in the maximum air velocity less than 0.28 %, in the oxygen consumption less than 0.07 %, in the minimum hydrogen mole fraction less than 0.05 %, in the methane conversion less than 0.03 % and in the average current density less than 0.09 % (compared with the predictions by 1 073 000 elements). It should be noted that the mesh is finest close to the electrode/electrolyte interface and the coarsest for the air- and fuel channels and for interconnects. The reason for such a mesh arrangement is mainly due to the charge transport and the electrochemical reactions (affecting the governing transport equations for ion, electron, mass, heat and momentum) appearing only in the regions close to the electrode/electrolyte interface.

The model relies on the experimental data from a standard cell developed at NIMTE in China. An ungraded case (case A) is defined with a cell voltage of 0.7 V, an oxygen utilization of 13 % and a fuel utilization of 71 %. As the graded structure is implemented the flow rates are kept constant, i.e., the fuel and oxygen utilizations are not specified directly for those cases. Some of the cell parameters used are given in Table 2. The differences between the different cases in the parameter study are outlined in Table 3. Notice, the parameters in Table 2 are kept constant in the parameter study.

Table 2: Cell parameters

Table 3: Parameters changed in the parameter study

SIMULATION RESULTS

The predicted temperature increases along the main flow direction (x-direction), as seen in Fig. 4, for the case with an ungraded structure. Heat is produced due to the different polarizations, the change of entropy due to electrochemical reactions in the cathode and the WGSR in the anode. On the other hand, heat is consumed due to the MSR as well as change of entropy due to the electrochemical reaction within the anode. It is found that the temperature and current density is strongly coupled and when any of them is changed, the other parameter will follow and the change is accelerated. A temperature difference is predicted in the y-direction inside the air channel because the convective heat flux in the air channel is bigger compared to the one in the fuel channel due to the relatively larger mass flow rate. An increased cell temperature will increase the cell current density. However, a too high temperature gradient or maximum temperature decreases the life time of the cell, due to material degradation and failure. For the case with an ungraded structure the current density increases along the main flow direction mainly due to an increased cell temperature. The increase is limited because of the decrease in OCV due to the temperature increase as well as the consumption of fuel and oxygen along the main flow direction.

The current density distribution along the y-direction (i.e., the direction normal to the main flow direction), at the inlet and outlet, in the cathode (to the left), electrolyte and anode (to the right) can be seen in Fig. 5 and along the x-direction (i.e., the main flow direction) in Fig. 6 (case A). Note that for the anode and cathode, only the parts (20 μm) closest to the electrolyte interface are included in Fig. 5. It can be seen that the current density gradients are steeper on the cathode side than on the anode side (Fig. 5). Notice, Fig. 6 includes the current density distribution for all the six investigated cases, but the results are discussed connected to each case, as they are presented below. The depth or thickness of the TPB region (in the direction normal to the main flow direction) is listed in Table 4 (for all cases investigated in the parameter study), where the thickness is defined as where 90 % of the electrochemical reactions occur. It should be noted that the behavior concerning the ion/electron current density, in the direction normal to the main flow direction, is similar for all cases, just the TPB thickness differs, which is the reason for presenting the comparison in a table. For the ungraded case the TPB thickness decreases from the inlet to the outlet, mostly due to an increased temperature, despite the increased current density. The cathode TPB is found to be thinner than the anode TPB. The depth of the active electrochemical reaction zones is quite small compared to the designed active layers (for example, 20 and 15 μm for the cathode and anode, respectively, for the NIMTE standard cell).

The mole fraction difference (*mfd,* in mol/mol) distributions at the direction normal to the main flow direction, within the anode (to the left) and in the fuel channel (to the right), at the outlet are shown in Fig. 7 and at the inlet in Fig. 8. The *mfd* is defined as the mole fraction at a specific position (in the direction normal to the main flow direction) subtracted by the mole fraction at the fuel channel/interconnect interface (eqn (33)), i.e., both positive and negative *mfd* values exist. The *mfd* is employed to compare the mole fraction distribution for several species (whose absolute mole fraction may differ in several orders of magnitude between different species) in the same plot. Both the OCV (i.e., the total amount of polarizations) and also the concentration polarization are dependent on the *mfd* distribution, i.e., it is critical for the cell performance. The concentration polarization is decreased from a decreased *mfd.* The OCV is increased by a high fuel mole fraction (hydrogen or carbon monoxide) and/or by a low electrochemical product mole fraction (water or carbon dioxide). The *mfd* for all cases investigated in the parameter study are presented in Table 5 and it should be noted that the behavior is similar for all cases, only the extremum values differs, which is the reason for presenting the comparison in a table. However, the discussion concerning the *mfd* is placed under each investigated case.

$$mfd_{i,y-dir} = x_{i,y-dir} - x_{i,fuel\ \text{channel/interconnect interface}} \tag{36}$$

The mole fraction of carbon monoxide decreases due to the electrochemical reaction with oxygen ions and the WGSR, and it reaches its lowest value at the anode/electrolyte interface. It should be noted that the WGSR proceeds towards the right within the entire anode, and the highest reaction rate can be found close to the outlet. However, this is not included in Figs 7-8. Hydrogen is produced in the WGSR and MSR, and consumed in the electrochemical reaction, with the lowest fraction found at the anode/electrolyte interface. Water is consumed in the MSR and WGSR and produced in the electrochemical reaction with hydrogen as fuel. The highest fraction can be found at the anode/electrolyte interface. Notice, water has the highest mole fraction difference between the anode/electrolyte interface and the anode/fuel channel interface, both at the inlet and at the outlet. Both the MSR and the electrochemical reaction with carbon monoxide as fuel produce carbon dioxide and the highest fraction is at the anode/electrolyte interface. Methane is only involved in the MSR and the lowest fraction is found at the anode/electrolyte interface. The *mfd* at the outlet are higher for the ungraded case for all species except for methane, due to the higher current density at the outlet, compared to at the inlet (as shown in Fig. 8).

The different polarizations for the ungraded case (case A) are presented in Fig. 9. The total amount of polarization at each location in the main flow direction depends on the OCV, which is affected by the local temperature and concentrations. The ohmic polarization due to ion and electron resistance increases along the main flow direction

(from 0.080 V at the inlet to 0.090 V at the outlet), due to an increased current density. This increase is limited by the simultaneous temperature increase. The concentration polarization within the cathode is neglible and relatively small within the anode. Note that the concentration polarization concerning carbon monoxide as fuel is slightly higher, than for hydrogen as fuel, resulting in a slightly lower activation polarization for the reaction including carbon monoxide, because only one OCV can exist. The activation polarizations dominate (among the different polarizations) and are strongly coupled to the current density. The activation polarization for the electrochemical reaction with hydrogen as reactant decreases from 0.128 V at the inlet to 0.075 V at the outlet.

Figure 4: Temperature distribution for the ungraded case (case A).

Figure 5: Profile of electron current density at the direction normal to the main flow direction at the inlet and outlet, for the cathode (to the left), the electrolyte and the anode (to the right), for the ungraded case (case A). Note that for the anode and cathode, only the parts (20 μm) closest to the electrolyte interface are highlighted in the figure and the "zero" is assigned at the air channel/cathode interface.

Figure 6: The current density distribution along the main flow direction (x-direction) for the six investigated cases.

Figure 7: Mole fraction differences (*mfd*) for water, hydrogen, methane, carbon monoxide and carbon dioxide in the anode (to the left) and fuel channel (to the right) in the direction normal to the main flow direction at the outlet for the ungraded case (case A). The actual mole fraction distribution can be calculated by adding the specific mole fraction for the actual species at the fuel channel/interconnect interface from Table 5 to the *mfd* value at the selected position and species within this figure (i.e., according to eqn (33)).

Figure 8: Mole fraction differences for water, hydrogen, methane, carbon monoxide and carbon dioxide in the anode (to the left) and fuel channel (to the right) in the direction normal to the main flow direction at the inlet.

Figure 9: Distribution of the different polarizations along the main flow direction for the ungraded case.

For the EAS being graded with the EAS inversely proportional to the x-position, the current density distribution is predicted along the main flow direction and presented in Fig. 6 (case B). The current density close to the inlet is increased, compared to the case without a graded structure, as presented in case A, due to an increased EAS in this region. On the other hand, the EAS is decreased close to the outlet and consequently the current density is reduced in that region. To summarize, the current density becomes smoother along the flow direction and the change between the current density at the inlet and the extremum is about 23 %, compared to 78 % for the case without a graded EAS. It should be noted that the same grading is applied within both the anode and the cathode, and also that the mean value of the EAS is identical as for the ungraded case (=1.00). It is clear that the temperature and current density is strongly related and when any of them is changed, the other follows and the change is accelerated. The TPB thickness decreases at the inlet (Table 4) compared to the ungraded case, due to the increased area available for electrochemical reactions. However, the TPB thickness increases at the outlet (Table 4), because the area available for electrochemical reactions is decreased, but the increase is limited from the decreased current density, compared to case A. The *mfd* between the TPB and the fuel channel interface increases (Table 5) at the inlet for all participating species, due to increased current density (electrochemical reaction rate). On the other hand the *mfd* between the TPB and the fuel channel interface decreases at the outlet for all participating species, because the current density is decreased, compared to case A. Note that the pore and particle radius are kept constant for this case. The increased *mfd* at the inlet decreases the total amount of voltage available for polarization, as shown in Fig. 10 (compared to Fig. 9). Consequently, a decreased *mfd* together with a decreased temperature at the outlet gives an increased sum of polarizations. The ohmic polarization (due to ion and electron transport) at the outlet increases to 0.097 V (compared to 0.090 V in case A), due to lower temperature and a thicker TPB. Also the hydrogen activation polarization at the outlet increases to 0.089 V (compared to 0.075 V in case A), because of the deceased EAS. However, this increase is limited from a decreased current density.

Figure 10: Distribution of the different polarizations along the main flow direction for the EAS graded case B.

The EAS is graded, with the EAS inversely proportional to the x-position along the main flow direction, according to case C in Fig. 2. The corresponding current density distribution is shown in Fig. 6 (case C). The change between the current density at the inlet and the extremum is about 3 %, compared to 78 % for the case without a graded EAS (case A). Note that the aim for this study is at a difference less than 5 %, to identify the impact from a graded

electrochemical structure along the main flow direction. The profile of the current density, in the direction normal to the main flow direction, is presented in Fig. 11, and compared to the case without a graded EAS in Fig. 5. It is found that the current density gradient (in the direction normal to the flow direction) is steeper at the inlet compared to at the outlet. However, this effect is not observed for the case with an ungraded structure. A steeper current density gradient is reflected by a thinner TPB thickness (see Table 4). The difference is due to the fact that more active surface sites are available close to the inlet when the grading is applied (case C compared to case A), i.e., the distance for the oxygen ions to be transported decreases despite an increased current density. At the outlet the decrease in EAS is partly compensated by the decrease in current density and the increase in TPB thickness is limited.

The temperature distribution for the case with optimized grading (case C) is presented in Fig. 12, to be compared to the case without a graded structure (case A) in Fig. 4. It is concluded that the total heat generation within the cell decreases, as the EAS is graded along the main flow direction. The difference between the maximum and the inlet temperature decreases from 87 K (in Fig. 4) to 72 K (in Fig 14). The average current density decreases from 6300 A/m^2 (case A) to 5900 A/m^2 (case C) as a consequence of the decreased cell temperature. To increase the cell current (or to maintain the same value as for the ungraded case) the temperature should be increased, for example, form a deceased air flow rate as performed in the case study presented later in this section. The *mfd* between the TPB and the fuel channel interface at the outlet is similar to case B, i.e., it is decreased compared to case A. However, at the inlet the *mfd* is increased in comparison to both case A and case B, due to the increased current density. The different polarizations along the main flow direction for case C is presented in Fig. 13. At the inlet the total amount of polarizations decreases from an increased *mfd*, due to the increased current density. The ohmic polarization at the outlet increases to 0.097 V (compared to 0.090 V in case A), due to lower temperature and a thicker TPB. Also the hydrogen activation polarization at the outlet increases to 0.092, compared to case A (0.075 V) as well as case B (0.089 V), because of the decreased EAS. However, this increase is limited from a decreased current density, when compared to case A.

Figure 11: Profile of current density at the direction normal to the main flow direction at the inlet and outlet for the cathode (to the left), the electrolyte and the anode (to the right), as the EAS is graded, according to case C.

Figure 12: Temperature distribution as the EAS is graded according to case C.

Figure 13: Distribution of the different polarizations along the main flow direction as the EAS is graded according to case C.

As the EAS is graded, along the main flow direction, also the particle- and pore radii are affected. Notice, that the pore and particle radii are kept constant for the investigated cases already presented in Figs 4-13 and also for the case to be presented concerning a decreased air flow rate, with the aim to study the impact from each parameter separately. In this part (presented in Figs 6 (case C pore and C MSR) as well as 16-17) the relationship between the EAS and the pore radius are investigated, defining the pore radius to be inversely proportional to the EAS, based on the assumption that the EAS is directly proportional to the active particle surface area. Note that the EAS is graded according to case C (in Fig. 2).

The current density distribution along the main flow direction for the case including both a graded structure of the EAS (case C) and of the pore radius (according to Fig. 3) is presented in Fig. 6 (case C pore). The decreased pore radius at the inlet increases the *mfd* between the TPB and the fuel channel interface (Table 5), compared to case C. It is found that the thickness of the TPB regions (Table 4) does not show any significant change, compared to case C. The pore radius is the smallest at the inlet and increases along the main flow direction, i.e., the mass transport resistance is bigger at the inlet and smaller at the outlet, which is the reason for a slightly lower current density at the inlet, due to an increased concentration polarization, to 0.008 V from 0.007 V concerning hydrogen as reactant (Fig. 14) and also a decreased OCV, compared to case C (Fig. 13). It is found that the average current density is 6000 A/m^2 (compared to 5900 A/m^2 in case C) and the difference between the inlet current density and the extremum is about 5 % (compared to 3 % with a constant pore size considered). The reason for the increased difference in current density between the inlet and the extremum is due to the fact that the grading is optimized for case C. The total polarization at the inlet is decreased compared to case C (Fig. 14), due to the increased *mfd*. At the outlet there is a small increase in the ohmic polarization to 0.099 V (due to slightly higher current density) and a small decrease in the activation polarization to 0.091 V, compared to 0.097 V and 0.092 V, respectively, for case C. The decrease in concentration polarization close to the outlet, due to the increased pore radius, is relatively small.

Figure 14: Distribution of the different polarizations along the main flow direction as the EAS as well as the pore radius are graded.

As the active MSR area-to-volume ratio is graded along the flow direction, the MSR rate increases close to the inlet, since more active surface sites are available. The current density (Fig. 6 (case C MSR)) decreases slightly close to the inlet (compared to case C EAS), due to the heat consumption in the MSR. A faster consumption of methane and a higher production of hydrogen as well as carbon monoxide close to the inlet (Table 5) increase the OCV and consequently also the current density along the main flow direction. The average current density is 6300 A/m^2, compared to 6300 A/m^2 for case A, 5900 A/m^2 for case C and 6000 A/m^2 for case C with additionally the pore radius graded. The difference between the inlet current density and the extremum is about 10 %, compared to 3 % for case C, for which the graded EAS is optimized. The maximum temperature increases to 1091 K (Fig. 15), compared to 1087 K for case A and 1072 K for case C.

Figure 15: Temperature distribution for the case with a graded EAS (case C), MSR (case C) as well as pore radius.

The last case study investigates the effect from a decreased air flow rate. The air flow rate is decreased with 21 %, compared to the case C, determined from the outlet temperatures (Fig. 16), which is the same as for case A. A decreased air flow rate decreases the cell cooling along the main flow direction and consequently the current density (Fig. 6 (case C air flow)) increases along the main flow direction, from the increased cell temperature, compared to case C. The average current density is 6200 A/m^2, compared to 6300 A/m^2 for the ungraded case A and 5900 A/m^2 for case C. The difference between the inlet current density and the extremum is about 10 %, compared to 3 % for case C, for which the graded EAS is optimized, i.e., it is recommended that a design optimization of the EAS should consider the expected operating conditions, including the air- and fuel utilizations as well as the fuel composition. The polarizations along the main flow direction are presented in Fig. 17 and it is found that the ohmic polarization increases at the outlet to 0.105 V (from an increased current density) compared to 0.097 V for case C and that the anode activation polarization decreases (to 0.084 V compared to 0.092) at the outlet. The *mfd* for hydrogen and water increases at the outlet (Table 5) compared to case C, due to the increased electrochemical reaction rate. The changes in TPB thickness (Table 4) are small compared to case C. An air flow rate reduction of 21 % means that less energy is needed for the air fan and also a decreased heat exchanger area required for the pre-heating of the air (with the exhaust gas recirculation).

Figure 16: Temperature distribution for the case with a graded EAS (case C) and additionally a reduced air flow rate.

Figure 17: Distribution of the different polarizations along the main flow direction as the air flow rate is reduced.

CONCLUSIONS

A CFD approach is developed and implemented to analyze various chemical and physical phenomena, which take place inside a single cell of an anode-supported SOFC. Both hydrogen and carbon monoxide are included as electrochemical reactants within the anode. Structural grading of the EAS, the active MSR area-to-volume ratio as well as the pore radius along the main flow direction is implemented to equalize the current density distribution along the main flow direction. It is found that the current density gradient, in the direction normal to the main flow direction, is steeper at the inlet compared to the outlet for the cases with a graded EAS, because more surface sites are available at the inlet, i.e., the average ion transport distance decreases. Note that the porosity and tortuosity are kept constant and ungraded within this work. The total sum of polarizations decreases along the main flow direction, because the OCV decreases, due to an increased temperature, a decreased fuel (hydrogen and carbon monoxide) concentration at the TPB and an increased electrochemical product (water and carbon dioxide) concentration at the TPB.

The grading effect of the particle and pore radius along the main flow direction is addressed in the parameter study. Due to the increase of the pore radius, along the main flow direction, the concentration polarization decreases slightly in the region close to the outlet, because the *mfd* between the TPB and the gas channel interface is decreased. The impact from pore and particle size grading on the TPB thickness is found to be small. As the MSR area-to-volume ratio is graded along the main flow direction, the OCV is increased from a higher electrochemical reactant concentration and lower electrochemical product concentration at the TPB region, close to the inlet.

It is predicted that a graded EAS structure reduces the cell current slightly if the fuel- and air flow rates are kept constant. However, a graded EAS (according to case C, i.e., neglecting the grading of the pore radius and the MSR active area-to-volume ratio) reduces the need of air flow rate with 21 %, compared to a cell without graded structure, when the outlet temperature is kept constant. As the air flow rate is changed, the difference between the current densities at the inlet and the extremum is increased from 3 % to 10 %, i.e., it is important that the operating conditions such as the air and fuel utilizations as well as the fuel composition are considered in the optimization process. A decreased air flow rate will reduce the heat exchanger area needed for pre-heating the air and also the energy required for the air fan. It is revealed that EAS grading along the main flow direction is an important step to design optimized

cells. A possible extension of the model presented in this paper includes simultaneous grading along the main flow direction and in the direction normal to the main flow direction, with focus on a decreased mass transfer resistance through the anode, i.e., an increased OCV.

NOMENCLATURE

AV surface area-to-volume ratio, m^2/m^3

c_p specific heat at constant pressure, J/kg/K

D_{ij} Maxwell-Stefan binary diffusion coefficient, m^2/s

$D_{k,ij}$ Knudsen diffusion coefficient, m^2/s

D_i^T thermal diffusion coefficient, kg/(m·s)

E (actual) operating voltage, V

E^0 open circuit voltage at standard pressure, V

EAS dimensionless number of electrochemical active sites, -

F volume force vector, N/m^3

F Faraday constant, 96485 C/mol

i volume current density, A/m^3,

k thermal conductivity, W/m/K or pre-exponential factor

K_{eq} equilibrium constant

mfd mole fraction difference, mol/mol

n number of species, -

p pressure, Pa or atm

Q_h source term (heat), W/m^3

R gas constant, 8.314 J/mol/K

r average particle/pore radius, m or reaction rate, mol/m^3

S_i source term (mass), $kg/(m^3s)$

T temperature, K

$\vec{u}$ velocity vector, m/s

w_i mass fraction of species i, kg/kg

x, y coordinate system, m

x_j molar fraction of species j, mol/mol

Greek symbols

β_F Forchheimer coefficient, kg/m^4

Ψ viscous stress tensor, N/m^2

τ tortuosity, -

σ ionic/electronic conductivity, Ω^{-1}m^{-1}

ρ density, kg/m^3

μ dynamic viscosity, Pa s

κ permeability, m^2

η polarization, V

ε_p porosity, -

ϕ potential, V

Subscripts and superscripts

a anode

act activation

avg average

b electrode/gas channel interface

c cathode

conc concentration

e electrode, $e \in \{a, c\}$, electrochemical

eff effective

el electrolyte material

ele electrolyte

g gas-phase

i molecule i

io electrode material

j molecule j

OCV open circuit voltage

ohm ohmic

Abbreviations

FC fuel cell

FEM finite element method

FVM finite volume method

LTE	local temperature equilibrium
LTNE	local temperature non-equilibrium
IEA	International Energy Agency
MSR	methane steam reforming reaction
NIMTE	Ningbo Institute of Material Technology and Engineering, China
SOFC	solid oxide fuel cell
TPB	three-phase boundary
WGSR	water-gas shift reforming reaction

Chemical

CH_4	methane
CO	carbon monoxide
CO_2	carbon dioxide
e^-	electron
H_2	hydrogen
H_2O	water
LSM	lanthanum strontium manganite
N_2	nitrogen
Ni	nickel
NO_x	nitrogen oxides
O^{2-}	oxygen ion
O_2	oxygen
YSZ	yttria-stabilized zirconia

ACKNOWLEDGMENT

The financial support from the Swedish Research Council (VR-621-2010-4581) and the European Research Council (ERC-226238-MMFCs) is gratefully acknowledged.

Table 1: Cell geometry

Cell Component	Thickness
Cell length	0.1 m
Fuel channel height	1 mm
Air channel height	1 mm
Anode thickness	415 μm
Cathode thickness	70 μm
Electrolyte thickness	10 μm
Interconnect thickness	300 μm

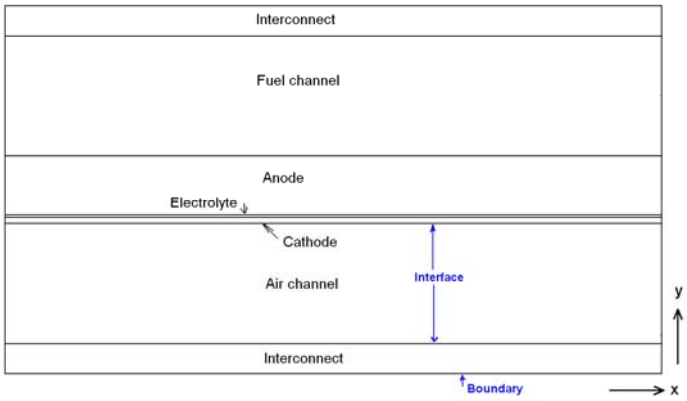

Figure 1: Sketch of an anode-supported SOFC, not to scale.

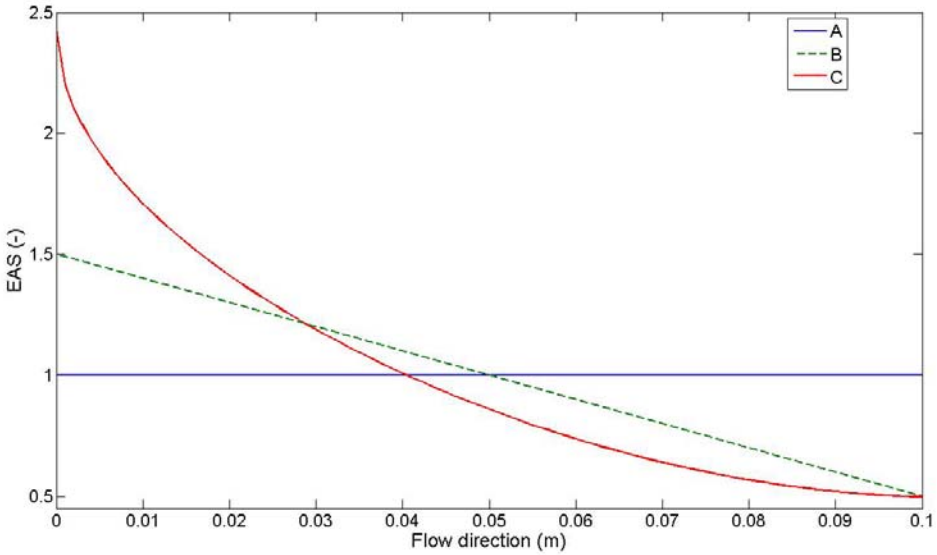

Figure 2: Grading the EAS along the main flow direction

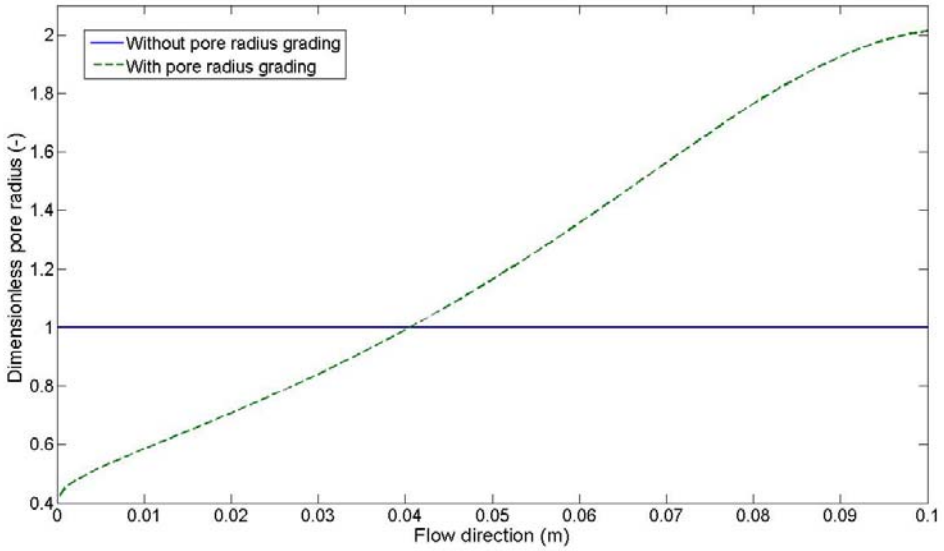

Figure 3: **Distribution of the dimensionless pore radius along the main flow direction, assuming that the pore radius is directly proportional to the active surface area, compared to the ungraded case.**

Table 2: Cell parameters

Inlet temperature	1000 K
Flow arrangement	co-flow
Ion conducting volume fraction	0.42
Electron conducting volume fraction	0.28
Porosity	0.30
Ion conducting tortuosity	10
Electron conducting tortuosity	10
Gas-phase totuosity	3
Cell voltage	0.7 V
Ungraded average pore radius	0.34 μm

Table 3: Parameters changed in the parameter study

Case	Air inlet velocity (m/s)	EAS grading	EAS-pore radius relationship	MSR active area-to-volume grading
A	2.10	-	-	-
B	2.10	B (Fig. 2)	-	-
C	2.10	C (Fig. 2)	-	-
C pore radius	2.10	C (Fig. 2)	C pore (Fig. 3)	-
C MSR	2.10	C (Fig. 2)	C pore (Fig. 3)	C (Fig. 2)
C dekr. air flow rate	1.66	C (Fig. 2)	-	-

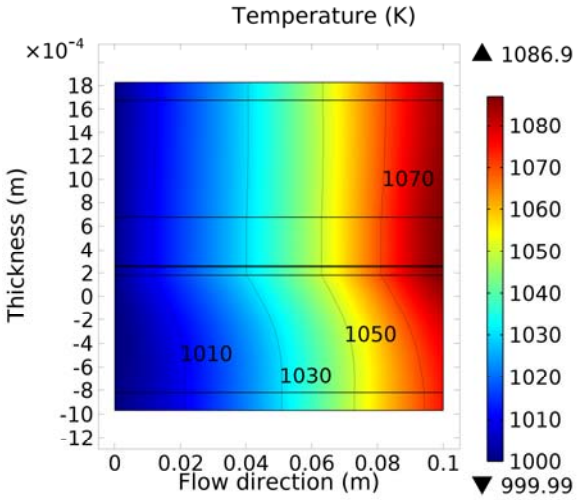

Figure 4: Temperature distribution for the ungraded case (case A).

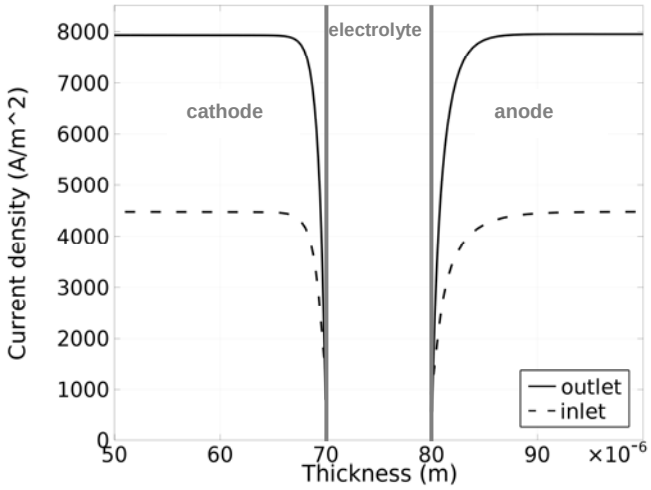

Figure 5: **Profile of electron current density at the direction normal to the main flow direction at the inlet and outlet, for the cathode (to the left), the electrolyte and the anode (to the right), for the ungraded case (case A). Note that for the anode and cathode, only the parts (20 μm) closest to the electrolyte interface are highlighted in the figure and the "zero" is assigned at the air channel/cathode interface.**

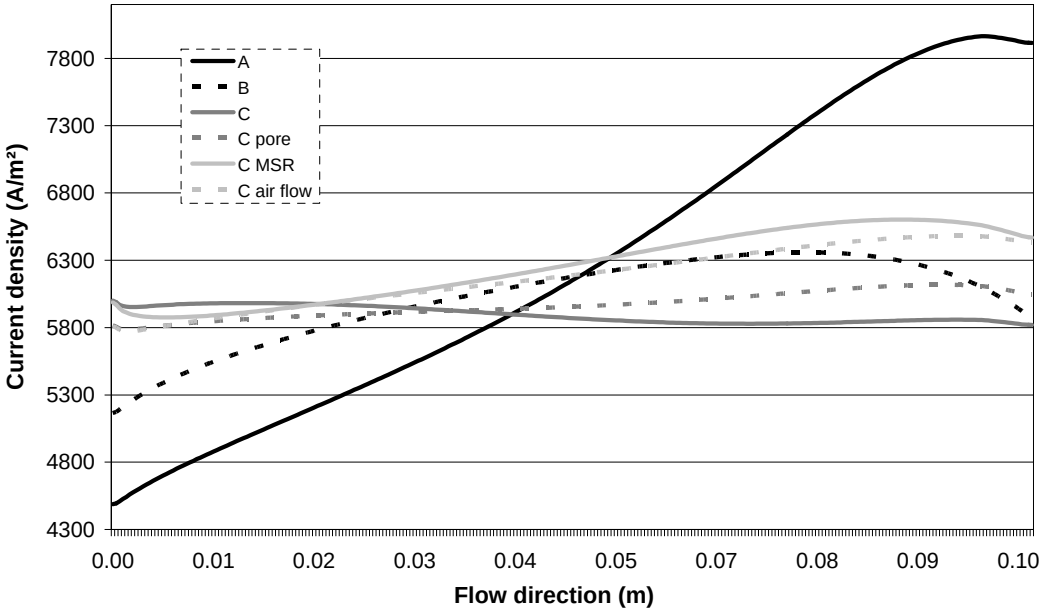

Figure 6: **The current density distribution along the main flow direction (x-direction) for the six investigated cases.**

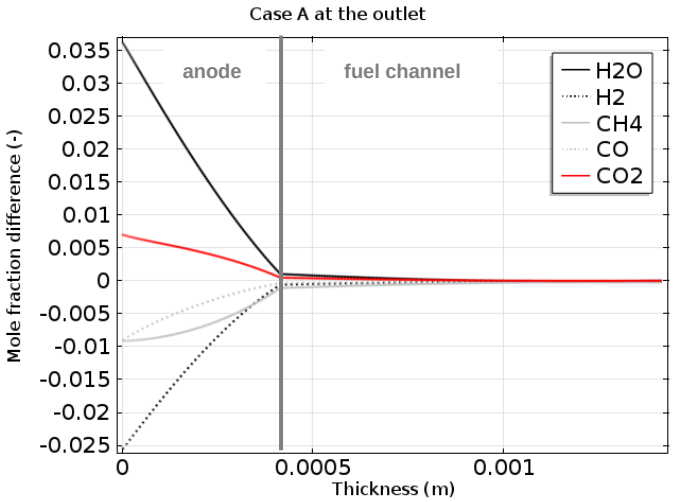

Figure 7: **Mole fraction differences (*mfd*) for water, hydrogen, methane, carbon monoxide and carbon dioxide in the anode (to the left) and fuel channel (to the right) in the direction normal to the main flow direction at the outlet for the ungraded case (case A). The actual mole fraction distribution can be calculated by adding the specific mole fraction for the actual species at the fuel channel/interconnect interface from Table 5 to the *mfd* value at the selected position and species within this figure (i.e., according to eqn (33)).**

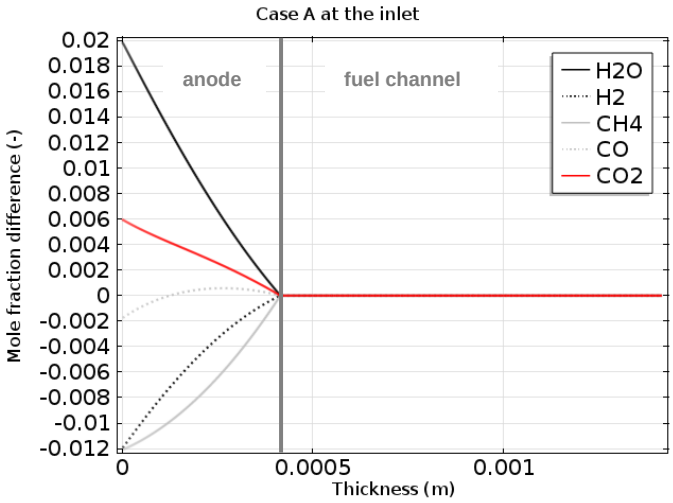

Figure 8: **Mole fraction differences for water, hydrogen, methane, carbon monoxide and carbon dioxide in the anode (to the left) and fuel channel (to the right) in the direction normal to the main flow direction at the inlet.**

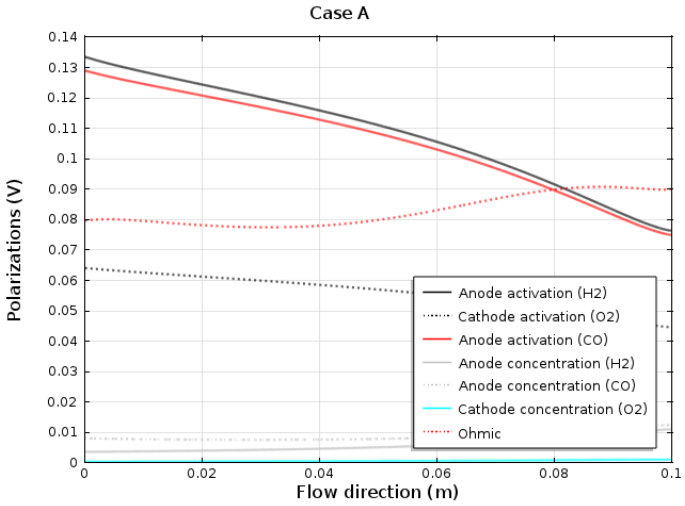

Figure 9: Distribution of the different polarizations along the main flow direction for the ungraded case.

Table 4: Thickness of TPB region (μm)

	Inlet		Outlet	
	Cathode	**Anode**	**Cathode**	**Anode**
A	1.7	3.6	1.5	2.5
B	1.4	2.8	2.1	3.7
C	1.0	2.4	2.0	3.7
$C_{\text{pore radius}}$	1.0	2.4	2.0	3.6
C_{MSR}	1.0	2.4	2.1	3.4
$C_{\text{flow rate}}$	1.2	2.5	2.2	3.6

Table 5: Mole fraction differences (*mfd in mol/mol*) and mole fractions (*x in mol/mol*)

			H_2	H_2O	CH_4	CO	CO_2
Outlet	**Mole fraction difference** between the anode/fuel channel interface and the TPB region	**A**	-0.0255	0.0365	-0.0087	-0.0085	0.0070
		B	-0.0175	0.0250	-0.0079	-0.0068	0.0063
		C	-0.0174	0.0250	-0.0078	-0.0067	0.0062
		C $_{\text{pore radius}}$	-0.0183	0.0221	-0.0057	-0.0053	0.0076
		C $_{\text{MSR}}$	-0.0207	0.0242	-0.0053	-0.0061	0.0074
		C $_{\text{flow rate}}$	-0.0195	0.0275	-0.0065	-0.0070	0.0063
	Mole fraction within the fuel channel	**A**	0.1505	0.6622	0.0229	0.0460	0.1190
		B	0.1620	0.6502	0.0250	0.0460	0.1176
		C	0.1672	0.6448	0.0260	0.0455	0.1170
		C $_{\text{pore radius}}$	0.1663	0.6461	0.0230	0.0453	0.1190
		C $_{\text{MSR}}$	0.1440	0.6665	0.0260	0.0420	0.1219
		C $_{\text{flow rate}}$	0.1752	0.6395	0.0183	0.0488	0.1184
Inlet	**Mole fraction difference** between the anode/fuel channel interface and the TPB region	**A**	-0.0120	0.0199	-0.0121	-0.0018	0.0059
		B	-0.0151	0.0245	-0.0130	-0.0022	0.0060
		C	-0.0192	0.0302	-0.0145	-0.0029	0.0062
		C $_{\text{pore radius}}$	-0.0259	0.0435	-0.0224	-0.0037	0.0082
		C $_{\text{MSR}}$	-0.0152	0.0332	-0.0341	0.0018	0.0143
		C $_{\text{flow rate}}$	-0.0180	0.0280	-0.0138	-0.0025	0.0060
	Mole fraction within the fuel channel	**All cases**	0.2626	0.4934	0.171	0.0294	0.0436

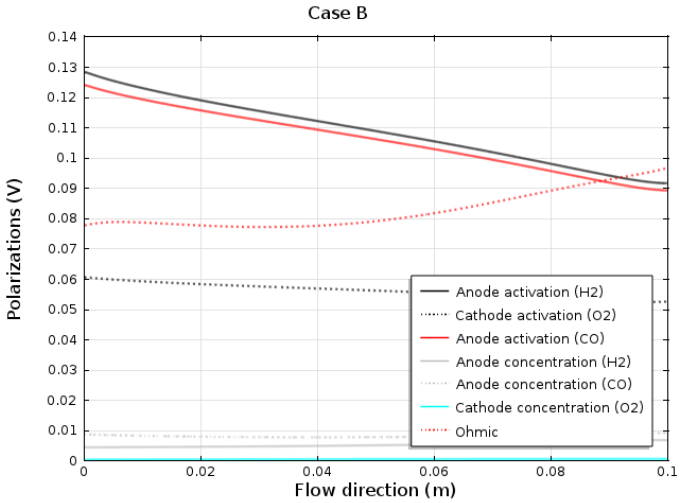

Figure 10: Distribution of the different polarizations along the main flow direction for the EAS graded case B.

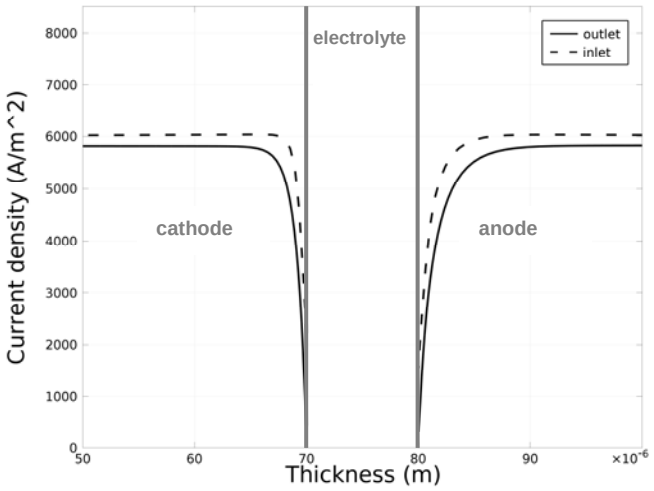

Figure 11: Profile of current density at the direction normal to the main flow direction at the inlet and outlet for the cathode (to the left), the electrolyte and the anode (to the right), as the EAS is graded, according to case C.

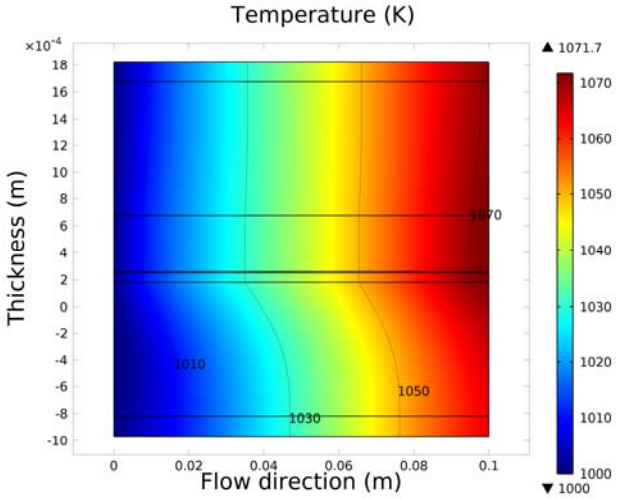

Figure 12: Temperature distribution as the EAS is graded according to case C.

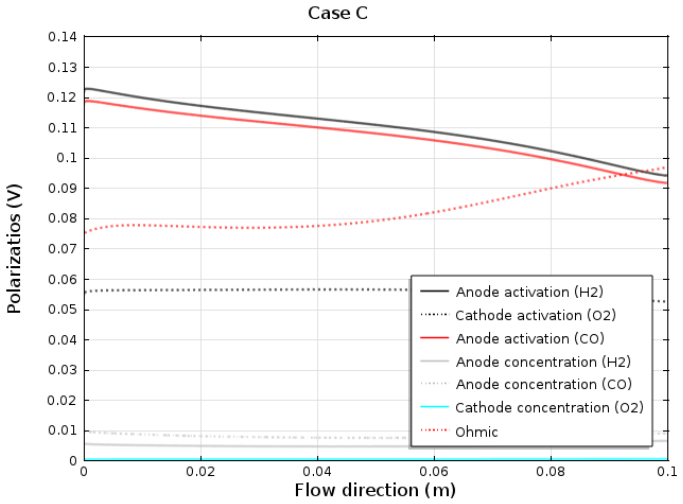

Figure 13: Distribution of the different polarizations along the main flow direction as the EAS is graded according to case C.

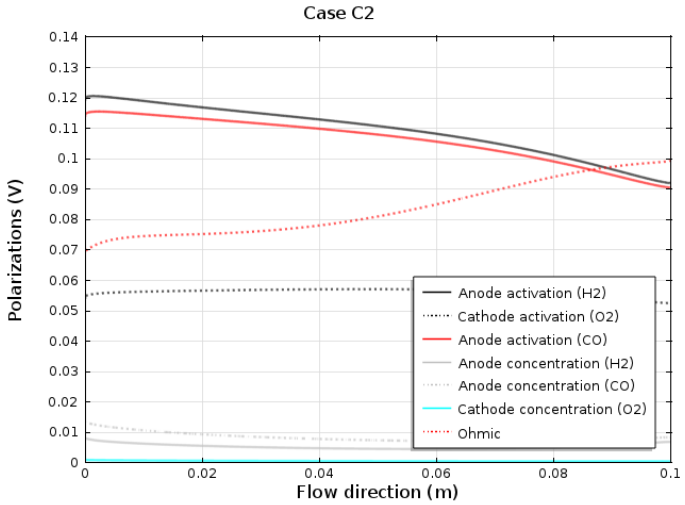

Figure 14: Distribution of the different polarizations along the main flow direction as the EAS as well as the pore radius are graded.

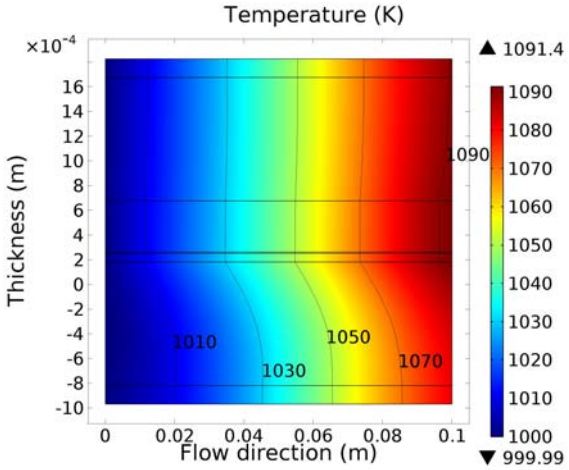

Figure 15: Temperature distribution for the case with a graded EAS (case C), MSR (case C) as well as pore radius.

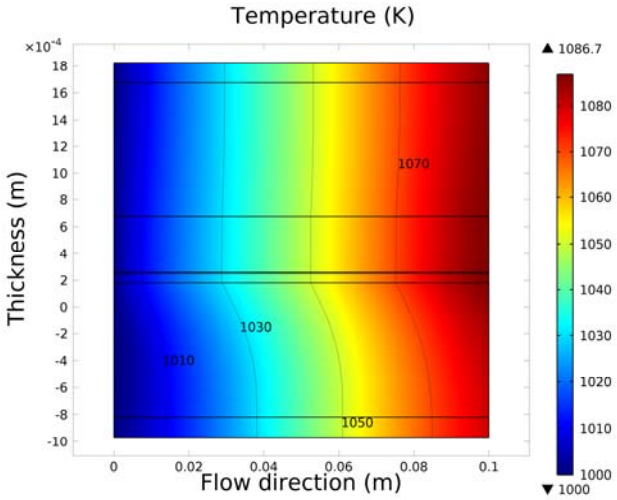

Figure 16: Temperature distribution for the case with a graded EAS (case C) and additionally a reduced air flow rate.

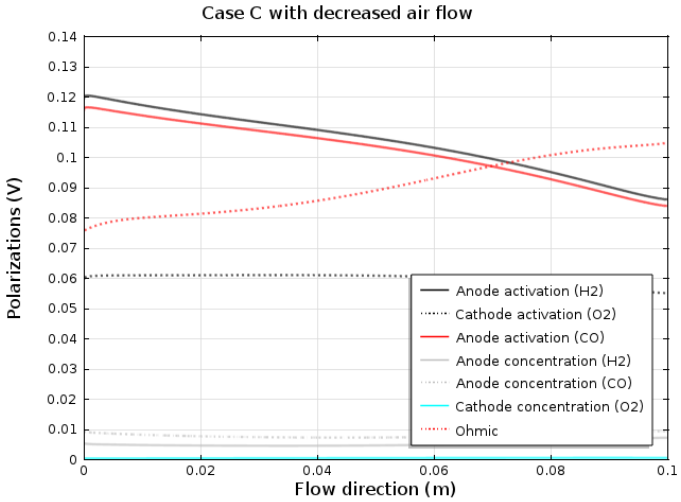

Figure 17: Distribution of the different polarizations along the main flow direction as the air flow rate is reduced.

REFERENCES

[1] J. Staniforth, M. Ormerod, *Catalysis Letter*, **81,** 19-23 (2002).

[2] V. Yurkiv, D. Starukhin, H.-R. Volpp, W.G. Bessler, *J. Electrochem. Soc.*, **158**, B5-B10 (2011).

[3] M. Andersson, Doctoral thesis, ISBN 978-91-7473-180-4, Lund University, Sweden (2011).

[4] M. Ni, M.K.H. Leung, D.Y.C. Leung, *J. Power Sources*, **168**, 369-378 (2007).

[5] V. Janardhanan, O. Deutschmann, *J. Power Sources,* **162**, 1192-1202 (2006).

[6] A. Ali, X. Wen, K. Nandakumar, J. Luo, K.T. Chunag, *J. Power Sources,* **185**, 961-966 (2008).

[7] L. Liu, R. Flesner, G.-Y. Kim, A. Chandra, *Fuel Cells*, **12**, 97-180 (2012).

[8] E.S. Greene, W.K.S. Chiu, M.G. Medeiros, *J. Power Sources*, **161**, 225-231 (2006).

[9] M. Ni, D.Y.C., Leung, M.K.H. Leung, *Energy Conversion and Management*, **20**, 268-278 (2009).

[10] J. Deseure, L. Dessemond, Y. Bultel, E. Siebert, *J. European Ceramic Soc.*, **25**, 2673-2676 (2005).

[11] L.C.R Schneider, C.L. Martin, Y. Bultel, L. Dessemond, D. Bouvard, *Electochim. Acta*, **52**, 3190-3198 (2007).

[12] J. Shi, X. Xue, *Electochim. Acta*, **55**, 5263-5273 (2010).

[13] Z. Wang, N. Zhang, J. Qiao, K. Sun, P. Xu, *Electrochemistry Communications*, **11**, 1120-1123 (2009).

[14] J.R. Ferguson, J.M. Fiard, R. Herbin, *J. Power Sources*, **58**, 109-122 (1996).

[15] S.A. Hajimolana, M.A. Hussain, W.M.A.W. Daud, M. Soroush, A. Shamiri, *Renewable and Sustainable Energy Reviews,* **15,** 1893-1917 (2011).

[16] Fuel Cell Handbook (7th edition), U.S. DoE, Morgantown, West Virginia (2004).

[17] W. Winkler, P. Nehter , *Fuel Cells and Hydrogen Energy*, **1**, 15-50 (2008).

[18] M. Ni, *Int. J. Hydrogen Energy*, **37**, 1731-1745 (2012).

[19] Y. Patcharavorachot, A. Arpornwichanop, A. Chuachuebsuk, *J. Power Sources*, **177**, 254-261 (2008).

[20] COMSOL Multiphysics 4.1 user guide, Stockholm, Sweden (2011).

[21] Fluent 12.1 user guide, Canonsburg, Pennsylvania, USA (2009).

[22] R. Suwanwarangkul, E. Croiset, E. Entchev, S. Charojrochkul, M.D. Pritzker, M.W. Fowler, P.L. Douglas, S. Chewathanakup, H. Mahaudom, *J. Power Sources*, **161**, 308-322 (2008).

[23] M. Kemm, Doctoral thesis, ISBN 91-628-6981-7, Lund University, Sweden (2006).

[24] M. le Bars, M.G. Worster, *J. Fluid Mech.*, **550**, 149-173 (2006).

[25] COMSOL Multiphysics 3.5 user guide, Stockholm, Sweden, 2008.

[26] H. Liu, P.R. Patil, U. Narusawa, *Entropy*, **9**, 118-131 (2007).

[27] M. Andersson, J. Yuan, B. Sundén*, Int. J. Heat Mass Transfer,* **55**, 773-788 (2012).

[28] J. Yuan, Y. Huang, B. Sundén, W.G. Wang, *Heat Mass Transfer*, **45**, 471-484 (2009).

[29] R.C. Reid, J.M. Prausnitz, B.E. Poling, The Properties of Gases & Liquids (fourth edition), McGraw-Hill Book Company, New York, USA (1987).

[30] D.Y. Murzin, T. Salmi, Catalytic Kinetics, Elsevier Science (2005).

[31] M. Andersson, H. Paradis, J. Yuan, B. Sundén, *J. Fuel Cell Sci. Technol.*, **8**, 031013 (2011).

[32] Y. Matsuzaki, I. Yasuda, *J. Electrochem. Soc.*, **147**, 1630-1635 (2000).

[33] M. Andersson, J. Yuan, B. Sundén, ASME ESFuelCell2011-54006 (2011)

[34] S.B. Beale, Transport Phenomena in Fuel Cells, Sundén and Faghri (eds.), WIT Press (2005).

[35] F. Bidrawn, R. Küngas, J.M. Vohs, R.J. Gorte, *J. Electrochem. Soc.*, **158**, B514-25 (2011).

[36] R. J. Gorte, J. M. Vohs, *Annual Reviews of Chemical and Biomolecular Engineering*, **2,** 9-30 (2011).

[37] H. Zhu, R.J. Kee, V.M. Janardhanan, O. Deutschmann, D.G. Goodwin, *J. Electrochem. Soc.*, **152**, A2427-A2440 (2005).

[38] J.-M. Klein, Y. Bultel, S. Georges, M. Pons, *Chem. Eng. Sci.*, **62**, 1636-1649 (2007).

[39] B.A. Haberman, J.B. Young, *Int. J. Heat and Mass Transfer*, **47**, 3617-3629 (2004).

[40] F. Nagel, T. Schildhauer, S. Biollaz, S.Stucki, *J. Power Sources,* **184**, 129-142 (2008).

[41] D. Sanchez, R. Chacartegui, A. Munoz, T. Sanchez, *Int. J. Hydrogen Energy*, **33**, 1834-1844 (2008).

[42] I. Drescher, W. Lehnert, J. Meusinger, *Electrochimica Acta*, **43**, 3059-3068 (1998).

[43] V. Danilov, M. Tade, *Int. J. Hydrogen Energy*, **34,** 8998-9006 (2009).

[44] D. Marrero-López, J.C. Ruiz-Morales, J. Peña-Martínez, J. Canales-Vázquez, P. Núñez, *J. Solid State Chemistry*, **181**, 685-692 (2008).